Advanced Intelligent Systems

ADVANCED INTELLIGENT SYSTEMS Open Access

www.advintellsyst.com

RESEARCH ARTICLE OPEN ACCESS

One-Shot Multimaterial 3D Printing of a Flexible Spine for a Robotic Fish Prototype

Marco Colletta[1,2] | Alessio Pricci[1,2] | Luca Di Leo[1,2] | Gianluca Percoco[1,2]

[1]Department of Mechanics, Mathematics and Management (DMMM), Polytechnic University of Bari, Bari, Italy | [2]Interdisciplinary Additive Manufacturing (IAM) Laboratory, Polytechnic University of Bari, Taranto, Italy

Correspondence: Alessio Pricci (alessio.pricci@poliba.it)

Received: 27 February 2026 | **Revised:** 7 April 2026 | **Accepted:** 8 May 2026

Keywords: 3D printing | electromagnetic actuation | FEM modeling | soft robots | tendon-driven transmission | biomimetics | robotic fish

ABSTRACT

Bioinspiration is shaping the development of next-generation robotic systems, particularly bioinspired swimmers capable of complex locomotion in unstructured environments at minimum energetic expense. However, their development is still limited by multistep fabrication processes requiring manual assembly of compliant and stiff components. This work proposes the one-shot multimaterial additive manufacturing (AM) of an electromagnetically (EM) actuated soft robotic fish capable of carangiform swimming, integrating polylactic acid (PLA) structural elements with a thermoplastic polyurethane (TPU) compliant spine through interlocked T-shaped interfaces. Three TPU grades (80A, 85A, and 95A Shore hardness) are evaluated to optimize actuation performance. Among them, the TPU 85A prototype achieves the highest tail-tip deflection while reducing the required actuation voltage (−46.67%), power consumption (−67.25%), and temperature rise (−47.68%). Finite element simulations of the soft robotic fish show good agreement with experimental bending behavior for all tested materials. Underwater tests performed across actuation frequencies from 0.5 to 5 Hz reveal a monotonic reduction in bending amplitude due to hydrodynamic load, while the mean tail-tip oscillation speed increases with frequency, reaching a 2.85× enhancement between the lowest and highest actuation frequencies.

1 | Introduction

Bioinspiration is a design paradigm that is gaining increasing relevance in the field of robotics, as mimicking living organisms allows engineers to benefit from millions of years of biological evolution, resulting in more efficient and higher-performing systems. This approach has been successfully applied to a wide range of robotic scenarios, including snake-inspired locomotion [1–4], aerial robotics [5, 6], and underwater applications [7–9].

In recent years, bioinspired robotic fish designs have been proposed to explore the marine environment [10, 11]. Within this context, the available literature designs can be classified into two main categories: systems that are (i) predominantly based on rigid components [12–14] or (ii) extensively exploit the unmatched properties of soft materials [15–19]. While the first typically offer more precise and repeatable motion control at the expense of a limited body compliance, the latter use soft materials to enhance flexibility, achieve smoother undulatory motion, and unlock the possibility to navigate through narrow channels [7].

3D printing has been increasingly adopted in soft robotics to fabricate compliant and increasingly challenging bioinspired designs [15, 20, 21]. When manufacturing soft robotic fish, however, 3D printing has been mainly used to produce rigid internal components and external shells [15, 22]. Flexible elements found in real fish, such as tails and spines, are often fabricated by casting elastomeric materials (e.g., silicones) into 3D-printed molds.

As a result, actual soft robotic fish designs have not yet been fully manufactured through a single monolithic manufacturing process, which is one of the key pillars for the advancement of 3D printing.

Most soft robotic fish designs rely on tendon-driven actuation powered by stepper or servo motors, which provide high responsiveness and controllability, although their relatively large size and weight remain a limitation [15, 16, 18, 23]. One of the first examples of tendon-driven robotic fish was proposed in [15], where a servo motor pulls antagonistic cables routed through articulated rigid vertebrae, generating effective body undulation of the soft robotic fish. Instead of the rigid joints adopted in previous solution, in [18], a compliant tendon-driven robotic fish featuring a flexible backbone enabled smoother body deformation and improved adaptability. In [16], this approach was further extended by introducing a dual-motor tendon-driven architecture capable of producing both C-shaped and S-shaped body profiles, allowing more versatile swimming patterns. More recently, a tendon-driven robotic fish featuring a double-spine mechanism was developed [23], achieving high-frequency swimming and enhanced propulsion efficiency through the use of a flexible skin covering the articulated structure.

A promising alternative to tendon-driven systems powered by rotary motors was presented in [22] where the interaction between solenoids embedded in the robot's head and permanent magnets integrated within a flexible tail generates a thrust sufficient for forward propulsion. Nevertheless, this solution remains constrained by a predominantly rigid body structure.

Despite their effectiveness, all the aforementioned soft robotic fish share a common limitation, that is, the large number of components that must be manufactured separately and manually assembled. This significantly impacts scalability, repeatability, and overall manufacturing efficiency.

Pneumatically driven soft actuators have also been applied in underwater environments [24–26]. In this context, pneumatic soft robotic fish—whose main advantage is to achieve large continuous body deformations—are relatively simple to fabricate. However, they typically require compressors, which are bulky, noisy, and difficult to integrate into fully autonomous underwater platforms.

From a design perspective, pneumatic soft robotic fish often rely on internal chambers embedded within elastomeric bodies, where controlled pressure variations generate body bending through asymmetric expansion. This architecture enables intrinsically compliant structures that are able to comply with unstructured environments. Moreover, pneumatic actuation allows smooth and highly tunable deformation patterns, with the potential of better mimicking the propulsion strategies followed by real fish in nature without the extensive use of rigid joints typical of rigid prototypes.

Motivated by the challenges of multistep fabrication in current designs, this work introduces a novel soft robotic fish prototype, characterized by simplified manufacturing, enabled by the multimaterial extrusion additive manufacturing (AM). Additionally, an innovative actuation system has been proposed: Specifically, the rotary motors commonly used in related literature [15] have been replaced by a pair of compact and programmable linear electromagnetic (EM) actuators, while still keeping a tendon-driven transmission mechanism to convert the EM force into an oscillatory motion of the soft tail.

While in [22], both actuation and motion transmission rely on EM interaction, in this work, these functions are decoupled: EM actuation is first converted into linear motion and then mechanically transferred along the body via a tendon. Furthermore, in [22], permanent magnets external to the coils are employed, whereas in present configuration, no permanent magnets are used. Instead, a ferromagnetic core is placed inside the solenoids, thereby allowing to leverage the stronger magnetic field within the coil to enhance force generation and stroke.

After proving the suitability of the aforementioned actuation system, the manufacturing process was selected to enable fully automated, one-shot 3D printing of the prototype.

Therefore, the proposed architecture addresses one of the main barriers to the industrial deployment of soft robotic systems, namely, the need for multistage fabrication workflows involving molding, bonding, and manual assembly of heterogeneous compliant and rigid components.

By embedding structural compliance directly within a multimaterial additively manufactured backbone, the present design enables the monolithic fabrication of an actuation-ready robotic structure in a single production cycle. This approach eliminates traditional hinge-based joints and postprocessing bonding operations, thereby reducing part count, assembly time, and operator-dependent variability while increasing manufacturing repeatability and process scalability.

In this regard, Table 1 provides a comparison of the manufacturing methodology for soft/stiff components and the actuation system with respect to current literature designs.

In addition, three soft materials—characterized by different Shore hardnesses—were selected for the production of the flexible spine. Numerical simulations were compared against experimental tests of the 3D-printed prototypes to find (i) the most suitable material for multimaterial 3D printing of the proposed design and (ii) the optimal actuation voltage. The optimized combination of soft material and actuation voltage was tested both in air and underwater. Specifically, for underwater tests, the usage of different actuation frequencies allowed to study the kinematic behavior of the tail and its dynamic interaction with the surrounding fluid.

The remainder of this article is organized as follows: Section 2 describes the prototype design, materials, actuation system, fabrication process, finite element settings, and testing setup. A direct comparison of the bending performance under different printing materials of the soft components with numerical results in air was provided in Section 3.1, together with the thermal analysis of the EM actuators. Dynamic tests were performed for the optimal material in underwater environment, under different actuation frequencies. Finally, conclusions and further works have been drawn in Section 4.

TABLE 1 | Manufacturing methods and actuation systems employed in current soft robotic fish prototypes.

Reference	Rigid component fabrication	Soft component fabrication	Mechanical assembly complexity	Electronic assembly complexity	Body manufacturing	Actuation System
[15]	3D printing	Silicone casting	High	High	Multistep	Servo motors + tendon-driven compliant tail
[22]	3D printing	Silicone casting	Medium	Medium	Multistep	Solenoids + compliant tail with integrated magnets
[23]	3D printing	3D printing	High	High	Multistep	Brushless motors + tendon driven tail
This work	3D printing	3D printing	Low	Medium	Single step	Solenoids + tendon-driven compliant tail

2 | Materials and Methods

2.1 | Design

The design process began with the identification of the target locomotion strategy, informed by the advantages and limitations of each swimming mode observed in biological fish. Specifically, a carangiform locomotion was selected because of its favorable balance between high swimming speeds and maneuverability [27]. Fish that exhibit carangiform locomotion are typically characterized by laterally compressed bodies that generate propulsion via periodic oscillations of the flexible posterior region of the body. Accordingly, the proposed prototype features a laterally compressed body, with the posterior part composed of rotating vertebrae interconnected by a compliant backbone that extends from the head to the peduncle, where the tail is attached (Figure 1).

In addition, the underside of the robot was designed to be flat in order to improve stability when the fish is at rest or moving at low speed near the seabed, thereby reducing the risk of unintended tilting or rolling. A flat bottom also facilitates stable support of the robot during 3D printing, electronic component assembly, testing, maintenance, and transport operations. The laterally compressed body and flat underside contributed to the realization of a self-supporting design (i.e., one that does not require support structures during the printing process).

From a manufacturing standpoint, the reduction of discrete mechanical joints and postassembly operations enabled by the proposed multimaterial extrusion process represents a key step toward scalable soft-robot production.

Unlike conventional soft robotic fish that rely on cast elastomeric components assembled onto rigid internal frames, the present

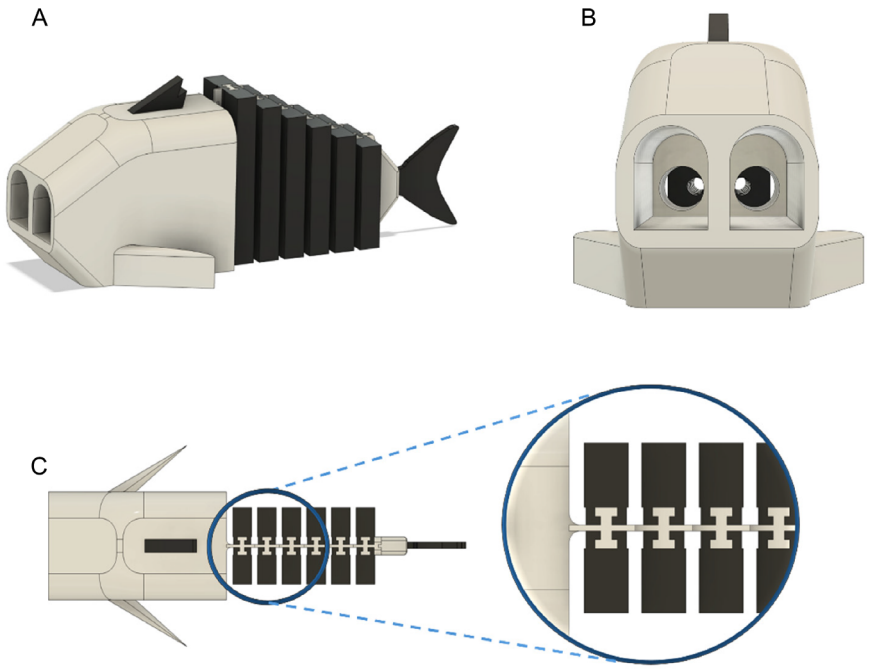

FIGURE 1 | (A) Design of the soft robotic fish. (B) Frontal view and (C) top view with indication of the interlocked soft-stiff structures.

solution integrates compliant and load-bearing structures within a single automated fabrication step. This not only minimizes dimensional variability introduced by manual assembly but also improves production repeatability and reduces the risk of mechanical misalignment between actuated components.

Computer-aided design (CAD) modeling of the robotic fish was performed in Autodesk Fusion 360, while toolpath generation for the multimaterial 3D printing process was carried out using Ultimaker Cura slicing software (v.5.10.0).

2.2 | Material and Testing Setup

Bioinspired design served also as the foundation for material selection. In fact, stiff and soft materials were assigned to body parts that exhibit lower and higher compliance in real fish, respectively.

Specifically, polylactic acid (PLA) was selected as the rigid material to manufacture the robot's skeletal components, while thermoplastic polyurethane (TPU) was used to fabricate the skin, cartilage, and muscles. The former includes the vertebrae and dorsal and caudal fin, whereas the latter are head, backbone, and pectoral fins (see Figure 1).

Three different TPU filaments were investigated, namely, Ninjaflex TPU 85A, Ultimaker TPU 95A, and BASF Ultrafuse TPU 80A Low Friction (LF). For each of the aforementioned TPU grades, the same design was fabricated and subsequently tested to evaluate the impact of material choice on the performance of the soft actuator (see Section 3). For all three prototypes, the rigid components were manufactured using BASF Ultrafuse PLA black. All materials were purchased in the form of 2.85 mm diameter filaments.

The mechanical behavior of each material was characterized by printing dogbones for uniaxial tensile testing according to ASTM D638 Type IV and testing them using an Instron 34TM-10 with a crosshead speed of 50 mm/min (see Section S1).

2.3 | Actuation System

The vast majority of robot fish designs proposed in literature adopt either (i) tendon-driven actuation systems pulled by a rotary servomotor or (ii) EM actuation systems. EM linear actuators are highly compact and easy to control, as they feature a reduced number of components.

However, fish swimming relies on undulatory movements of the tail, and tendon-driven actuation is particularly suitable since it mimics the behavior of real fish muscles and transfers force along a flexible body without significantly increasing the mass of the prototype. Moreover, this design choice allows actuators to be placed away from the moving parts, thereby reducing the inertia of components subjected to continuous motion, such as the vertebrae and the tail.

In this work, an innovative hybrid actuation system was therefore adopted, combining the benefits of tendon-driven actuation with the simplicity of control of EM actuation. Specifically, motion is transmitted along the vertebrae via the tendon-driven system, while a linear actuation mechanism driven by solenoids embedded in the head of the soft robotic fish pushes and pulls the cable. The operating principle of this mechanism is illustrated in the sketch shown in Figure 2.

Two Heschen HS-0530B DC12V linear actuators were used as EM actuators. They feature a metal frame containing a fixed coil and an iron core. When the coil is powered, it generates a magnetic field that causes the core to slide forward, reaching up to 10 mm of stroke. The core can generate a pulling force of 5 N, as specified by the manufacturer [28]. When the current is removed, the magnetic field collapses and a helical spring restores the core to its initial position. The actuator incorporates a cylindrical ring that enables mechanical attachment of the cable, thereby eliminating the need for adhesive bonding or welding. The cable passes through the six vertebrae and is anchored to the last ones using locking plates. When the cable is pulled, the compliant spine bends, thereby inducing relative rotation among the vertebrae and a corresponding rotation of the tail. Alternating the power supply of the left and the right actuator selectively, the corresponding cable is pulled, producing leftward or rightward spinal bending and an alternating tail rotation.

2.4 | Prototype Fabrication

One of the main purposes of this work was to develop a design capable of minimizing the number of manual assembly steps,

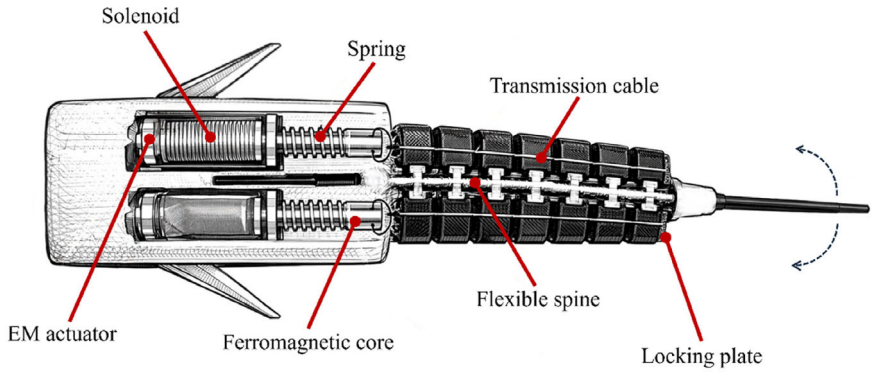

FIGURE 2 | Functional components of the EM-actuated soft robots.

which are inherently time-consuming and prone to errors. Thanks to the use of multimaterial 3D printing, the proposed prototype features a flexible TPU backbone fully connected to six rigid vertebrae manufactured in PLA. This choice made it possible to eliminate the traditional hinge joints used in most of the previously developed robot-fish prototypes [13, 15, 23, 29].

In multimaterial 3D printing, especially when combining materials with significantly different mechanical properties such as PLA and TPU, issues related to poor intermaterial adhesion, surface quality, and dimensional accuracy are commonly encountered. In this context, the use of a prime tower proved to be essential in ensuring multimaterial 3D printing with minimal material cross-contamination. Furthermore, a T-shaped interlocking profile [30] was implemented at the interface between the two materials in the vertebrae (see Figure 1C).

Another key factor that motivated the choice of 3D printing as the optimal manufacturing process is the reduction of material waste, which is considerable in traditional manufacturing methods, especially in subtractive processes. However, since material waste can occur also in 3D printing due to support structures, particular attention was devoted to the development of a self-supporting design both for the external structure and the internal housing of the electronic components.

An Ultimaker S5 dual-extruder FDM 3D printer, equipped with 0.4 mm nozzles was used to manufacture the proposed soft robotic fish. Both PLA and TPU filaments were dried for 24 h prior to 3D print using a SUNLU FilaDryer S2 to minimize the moisture content. The following process parameters were used to 3D print the soft robotic fish prototypes (Table 2).

2.5 | Finite Element Simulations

Numerical simulations were done with the finite element commercial software COMSOL Multiphysics v.6.2. The stress–strain relationship was modeled for each material using the properties outlined in Table 3.

The Young's modulus information was found by making the least-square fitting of the mean stress–strain curve for each tested material, in the linear-elastic regime (see Section S1).

The real material density was determined by cutting three specimens of 3 cm each from each filament spool. Then, these were weighed via an analytical balance (Practum 124-1S, Sartorius Lab Instruments GmbH & Co. KG, Goettingen, Germany; resolution: 0.1 mg), and their mean weight was divided by the cylinder volume.

The boundary conditions used in the finite element model were representative of the environment where the soft robotic fish was actuated (see Figure 3).

In particular, a load representative of an overall force of 5 N was applied to the boundary of the hole passing through the PLA vertebrae (red boundary in Figure 3). The bottom surface of the soft robotic fish was constrained with a roller boundary condition (i.e., the displacement in the direction orthogonal to the aforementioned surface was set to zero):

$$\vec{u} \cdot \vec{n} = 0 \tag{1}$$

where $\vec{u}$ is the displacement field and $\vec{n}$ is the unit vector orthogonal to the bottom surface.

Furthermore, the degrees of freedom associated with the head of the soft robotic fish were fixed (dark gray in Figure 3), to replicate the blockage realized in the experimental setup. Up to this part, the boundary and load conditions were common to both air and underwater applications (see Figure 3A).

However, the deformation achieved by the soft robotic fish underwater was expected to be different from the one in air

TABLE 2 | Main process parameters for the different 3D printing materials.

Material	Flow, %	Initial temp., °C	Final temp., °C	Printing temp., °C	Printing speed, mm s^{-1}	Retraction distance, mm	Infill speed, mm s^{-1}	Infill, %	Infill pattern
PLA	100	190	190	205	60	6.5	60	10	Grid
TPU 80A	106	235	200	245	25	6.5	25	15	Cross 3D
TPU 85A	106	240	230	245	25	8.5	20	15	Gyroid
TPU 95A	115	215	215	225	15	10	15	15	Gyroid

TABLE 3 | Material properties used in finite element simulations.

Material	Density, ρ, kg/m^3	Young's modulus, E, MPa	Poisson ratio, ν, –
PLA	1240	2600	0.35
TPU 80A	1238	28.93	0.38
TPU 85A	1289	23.19	0.36
TPU 95A	1270	58.21	0.39

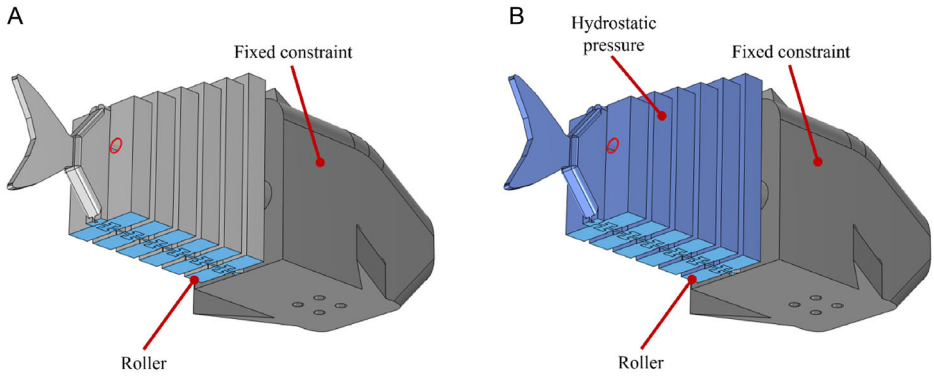

FIGURE 3 | Boundary conditions for the simulation of the EM actuated soft robotic fish in (A) air and (B) underwater environments.

because of the hydrodynamic resistance. To model the action of the fluid, hydrostatic pressure was applied to all surfaces (see Figure 3B):

$$p(z) = \rho_{H2O} g z \tag{2}$$

where ρ_{H2O} is water density, g is gravity, and z is the absolute depth position.

All the vertebrae of the soft robotic fish potentially undergo mutual interaction. For that reason, nonlinear contact pairs were modeled using the penalty contact formulation available in COMSOL. In this framework, normal contact traction acting on the interface (T_n) is computed as

$$T_n = \begin{cases} -p_n g_n & \text{if} g_n \le 0 \\ 0 & \text{if } g_n > 0 \end{cases} \tag{3}$$

where p_n is the penalty contact stiffness and g_n the normal gap between the source and destination boundaries. The former has been evaluated as

$$p_n = \tilde{f}_p(g_n) \frac{E_{\text{char}}}{h_{\min}} \tag{4}$$

where $\tilde{f}_p(g_n)$ is a gap-dependent penalty factor multiplier, E_{char} is the characteristic Young's modulus of the contacting materials, and $h_{\min}$ is the minimum mesh element size in the contact region, used to scale the contact stiffness. In particular, $\tilde{f}_p(g_n)$ can be written as

$$\tilde{f}_p(g_n) = \begin{cases} f_{p,\text{fin}} - \left(f_{p,\text{fin}} - f_{p,\text{init}}\right) \frac{g_{n,\text{tr}}}{g_n} & \text{if } g_n \le g_{n,\text{tr}} \\ f_{p,\text{init}} & \text{if } g_n > g_{n,\text{tr}} \end{cases} \tag{5}$$

where $f_{p,\text{init}}$ and $f_{p,\text{fin}}$ are the initial and final value of the penalty factor multiplier, equal to 10^{-2} and 1, respectively, while $g_{n,\text{tr}}$ is the transition gap used to ramp the penalty factor smoothly during contact enforcement.

An unstructured computational mesh was gradually refined until grid-independent results were achieved (see Section S2). In particular, a mesh size consisting of 204 353 elements provided accurate results both in air and underwater simulations.

2.6 | Experimental Setup

To evaluate the robot's performance, it was placed on a flat surface, and its tail was actuated to measure maximum bending, rotation angle, peak deflection, and the evolution of tail position with time. To do this, a PLA mounting plate was designed to fit into holes positioned beneath the robot's head and secured to a table using a bench vise.

This setup allowed to accurately track the robot's movements via a recording camera (Canon EOS 400D, Canon, Japan) positioned above the soft robotic fish, thus capturing the periodic lateral bending.

The robot's actuators were powered using a bench power supply EA-PS 2000B, while an Arduino Uno board was powered via a laptop with a constant 5 V supply and connected to a relay module in order to switch the supplied EM actuator (see Figure 4).

Additional tests were performed using a Fluke PTi120 thermal camera to monitor the maximum temperature reached by the system.

For the underwater experiments, the robot was placed in a transparent basin ($60 \times 58 \times 16$ cm), filled with water to a depth of 10 cm. Also in this case, the digital camera was mounted above the robot to record its movements from a top-view perspective. The robot was mechanically constrained by inserting a PLA plate into the holes located beneath its head and then fixing that plate to the bottom of the basin.

3 | Results and Discussion

3.1 | Tail Characterization in Air

Three robotic fish prototypes sharing the same geometry and mechanical components highlighted in Section 2, while differing in the soft material being used to 3D print the compliant elements, were tested. This approach enabled a systematic evaluation of the influence of material properties on the mechanical behavior of the soft robot.

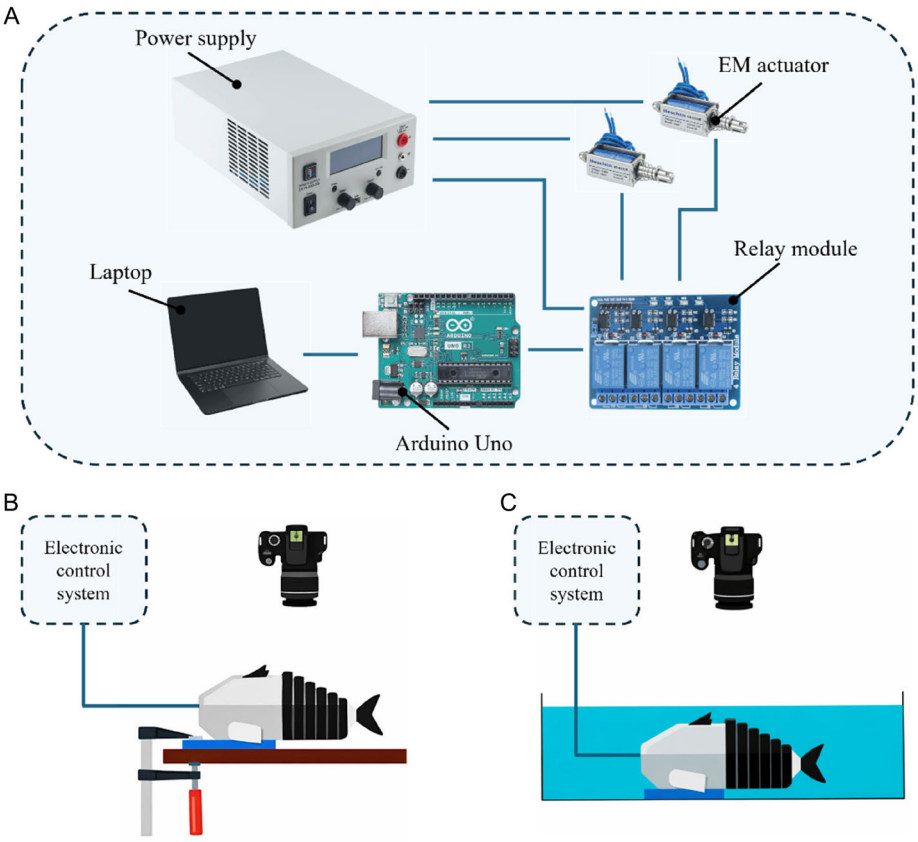

FIGURE 4 | (A) Electronic control system of the EM actuator and details of the experimental setup used for (B) air and (C) underwater tests.

3.1.1 | Bending Performance in Air and Material Selection

For each prototype, experimental tests were performed to evaluate the achievable maximum bending. The supply voltage needed for the robot's actuation was adjusted depending on the soft material chosen for the printing process. From preliminary tests, the Ninjaflex TPU 85A prototype already reached its maximum bending (i.e., the condition in which vertebrae come into contact) at 6.9 V, whereas neither the TPU 80A LF nor the TPU 95A model achieved the aforementioned condition even though operating at 12 V, which is the actuators' voltage limit. Therefore, for the latter two prototypes, the supplied voltage was set equal to 12 V, to achieve the highest possible bending. Among the three prototypes, the largest bending was achieved by the one produced in TPU 85A. Then, an intermediate bending performance was achieved by the TPU 80A LF prototype, while the TPU 95A configuration exhibited the lowest one (see Figure 5).

From both experimental and numerical standpoints, virtual markers were placed (i) on the soft robotic fish head, (ii) in the center of each vertebra, and (iii) on the tail tip, to track the robot deformation when actuated (see Figure 6A). This allowed to make a consistent comparison between FEM and real soft robotic fish deformations.

In particular, the TPU 80A LF prototype achieved a peak lateral tail-tip displacement of 47.10 mm relative to the body midline, corresponding to a maximum bending angle of 34.1° during leftward actuation, and 48.30 mm with a maximum bending angle of 34.7° during rightward actuation, resulting in a rotational asymmetry of 1.73%. The TPU 85A prototype exhibited larger deflections, reaching 65.24 mm (maximum bending angle of 56.9°) when actuated leftward and 63.83 mm (maximum bending angle of 56.3°) during rightward actuation, yielding the lowest asymmetry value of 1.07%. Conversely, the TPU 95A specimen showed reduced motion, with a peak displacement of 36.27 mm corresponding to a maximum bending angle of 27.9° during leftward actuation and 33.14 mm with a maximum bending angle of 27.2° during rightward actuation, leading to a rotational asymmetry of 2.51%.

The numerical results agree well with experiments, especially when it comes to the lowest (TPU 80A LF) and the highest (TPU 95A) Shore hardnesses. The parabolic-like curvature induced by the load exerted by the EM actuators was accurately reflected by the finite element results shown both in Figures 5 and 6. Moreover, the maximum absolute deflection achieved by the tail in experiments was equal to 48.30, 65.24, and 36.27 mm, for the TPU 80A LF, TPU 85A, and TPU 95A, respectively. Finite element simulations yielded deflections of 47.10 mm (2.48%), 65.45 mm (0.32%), and 35.26 mm (2.78%) for the aforementioned materials, showing very good correspondence with experimental data.

Among the three materials investigated, TPU 85A exhibited the most favorable mechanical response. Specifically, it required a lower actuation energy, while enabling a significantly greater bending capability. In addition, the rotational response measured at the tail tip showed minimal asymmetry between left and right

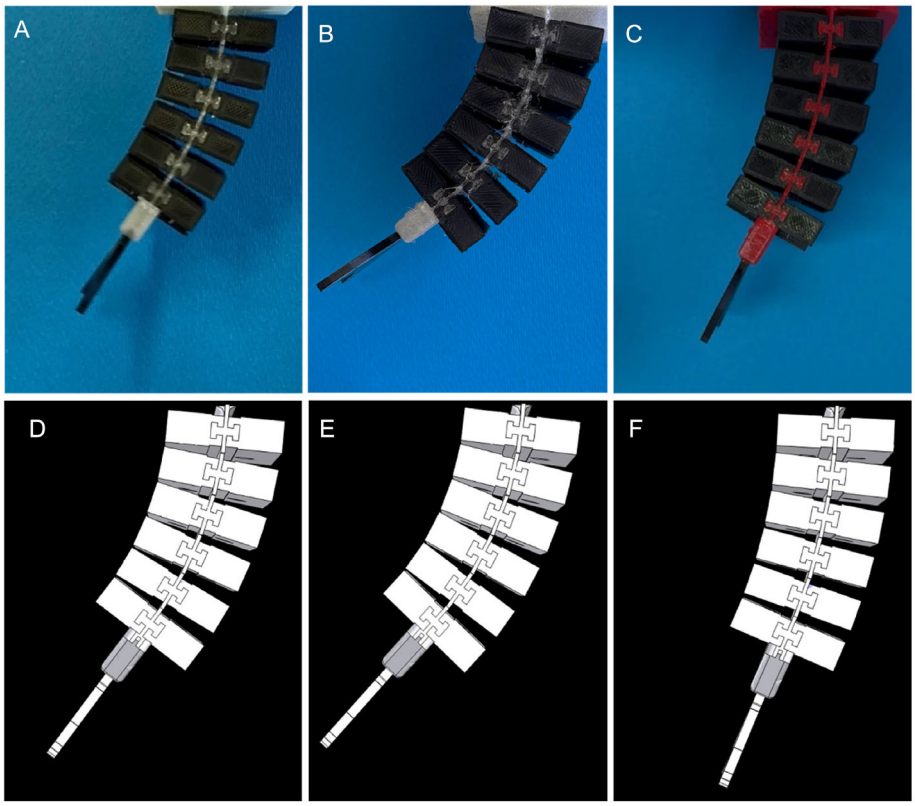

FIGURE 5 | Experimental test of the EM actuation of the soft robotic fish using (A) TPU 80A LF, (B) TPU 85A, and (C) TPU 95A for the compliant section, together with the numerical comparison of (D) TPU 80A LF, (E) TPU 85A, and (F) TPU 95A curvature found via finite element simulations.

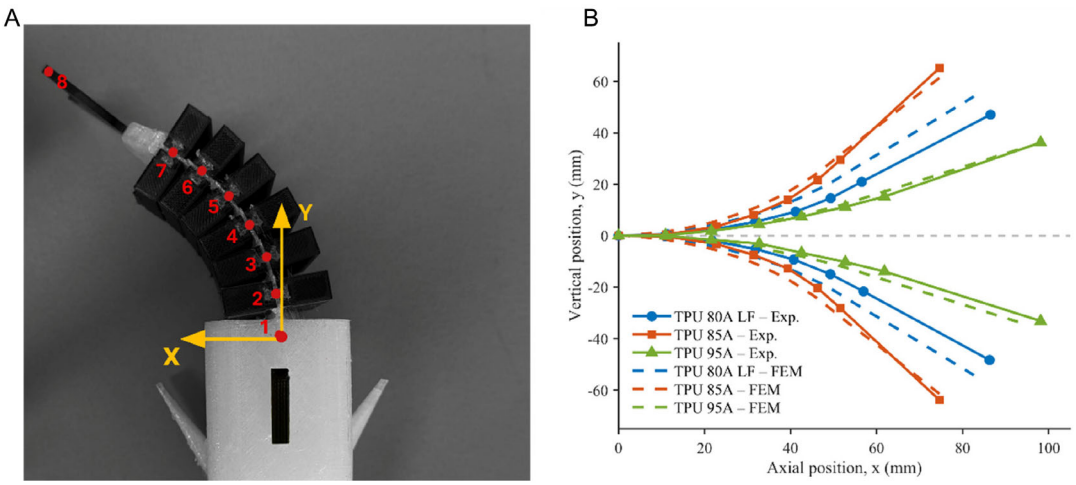

FIGURE 6 | (A) Reference system and virtual markers used for the experimental and numerical analysis of the soft robotic fish EM actuation; (B) comparison of experimental and numerical results for the different soft materials adopted for the 3D printing of the compliant spine.

rotations when compared to the other materials. The bending asymmetry was imperceptible when simulated via finite elements because of the perfect load and geometrical symmetry.

3.1.2 | Thermal Behavior of the Selected Material

Heat generation was evaluated at the two voltage levels adopted in this study (i.e., 6.9 and 12 V). The robot was actuated for a duration of 5 min, while temperature evolution was continuously monitored using the thermal camera. Both the temporal temperature behavior and the spatial heat distribution across the robotic structure were monitored and analyzed. At the beginning of each experiment, the actuators' temperature was 24°C. When actuated at 6.9 V, the prototype exhibited a gradual temperature increase, reaching a maximum of 48.4°C. Instead, actuation at 12 V resulted in a steep temperature profile, reaching a peak value of 92.5°C.

Furthermore, thermal analysis revealed that the maximum temperature was not localized on the actuators themselves, but

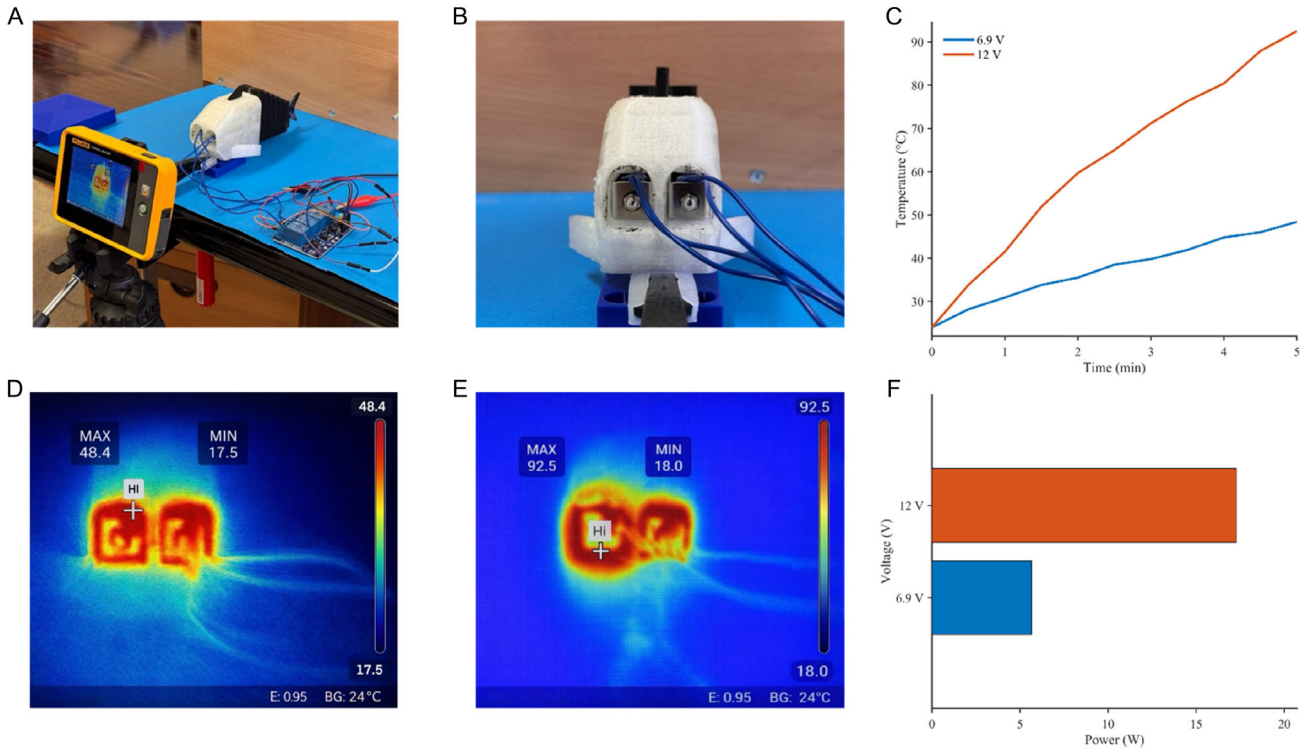

FIGURE 7 | (A) Testing setup for the thermal imaging. (B) Frontal view of the 3D-printed actuator with detail of the EM actuator positioning for test in air. (C) Temperature history at different actuation voltages. (D) Thermal field at 6.9 V. (E) Thermal field at 12 V. (F) Power required for the EM actuation at the two investigated voltages.

rather in the TPU housing region where the actuators are embedded. This trend was consistently observed for both voltage levels, as highlighted by the thermal images (see Figure 7A–E), indicating a nonuniform heat distribution across the robot's structure.

In addition to thermal measurements, electrical power consumption was also evaluated for both actuation conditions (see Figure 7F). When operated at 6.9 V, the prototype exhibited an average power consumption of 5.66 W. Actuation at 12 V resulted in a significantly higher power consumption of 17.28 W (i.e., increase of 53.32%).

This combination of reduced energy demand, enhanced bending performance, and near-symmetric rotational behavior identifies TPU 85A as the most mechanically efficient and balanced material within the tested set. Based on these results, TPU 85A was selected as the reference material and was therefore exclusively employed in all subsequent experimental tests.

3.2 | Dynamic Tests and Bending Performance in Water

The performance of the soft robotic fish in water was evaluated through dynamic tests, where each test was characterized by a specific actuation switching frequency. To reproduce the typical oscillatory motion of the tail used by real fish for locomotion, the power supply was alternated between the left and right actuator. By varying the frequency of this power-supply switching, different tail oscillation frequencies were obtained. The selected frequencies were 0.5, 1, 2, 3, 4, and 5 Hz. These dynamic tests were conducted both in air and in water. During the tests in air, the maximum bending of the spine allowed by the geometry was reached at all the investigated frequencies (see the results reported in Section 3.1.1). In contrast, during the tests in water, the maximum bending was never achieved, and the overall bending amplitude was observed to depend on the actuation frequency (see Figure 8).

The highest bending measured in water occurred at an actuation frequency of 0.5 Hz and was confirmed by the finite element results coming from the simulation of the hydrostatic load on soft robotic fish external surfaces (Figure 8A–C). However, the corresponding curvature was substantially lower compared to the air test (see Section S3). As the oscillation frequency increased, the maximum curvature progressively decreased, reaching its minimum at the highest investigated frequency of 5 Hz (Figure 8D).

The most pronounced reductions in bending were observed in the frequency transitions from 0.5 to 1 Hz, from 1 to 2 Hz, and from 2 to 3 Hz, whereas only minor reductions were recorded for the subsequent increases from 3 to 4 Hz and from 4 to 5 Hz. Specifically, the peak tail-tip displacement decreased by 5.84, 11.32, and 8.66 mm across the 0.5–1, 1–2, and 2–3 Hz transitions, respectively, while reductions of only 1.86 and 1.20 mm were measured for the 3–4 and 4–5 Hz frequency increments. This trend, characterized by larger oscillation amplitudes at low frequencies, is consistent with the locomotion dynamics observed in real fish [31].

The observed behavior can be attributed to the combined effects of fluid–structure interaction and actuator dynamics. In fact, the

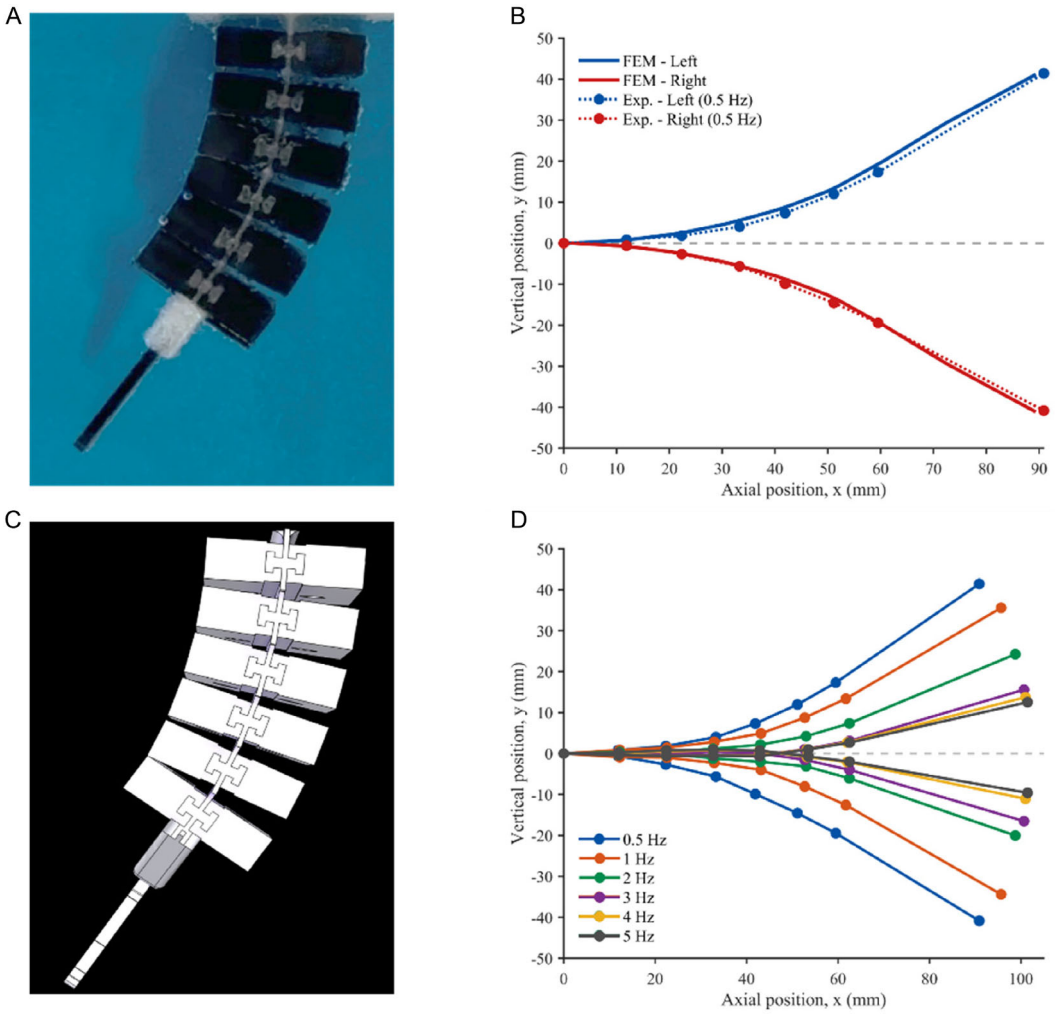

FIGURE 8 | (A) Experimental view of the body deflection under 0.5 Hz of actuation frequency in underwater tests. (B) Comparison with finite element results. (C) Numerically computed body curvature. (D) Dependence of body curvature from actuation frequency.

surrounding water introduces significant inertial and viscous loads that oppose rapid structural deformation driven by the soft spine compliance. At low actuation frequencies, the system has sufficient time to overcome hydrodynamic resistance and approach its maximum achievable curvature, while still being limited in magnitude because of the hydrostatic load. However, the time available for bending decreases with increasing switching frequency, and the actuators are no longer able to fully deform the spine before the energized EM actuator is switched.

The percentage oscillation asymmetry—defined as the relative difference between the maximum leftward and rightward tail rotation angles—was also evaluated and found to increase with actuation frequency. At 0.5 Hz, the peak lateral tail-tip displacement measured on the left side was 41.42 mm, corresponding to a maximum tail-tip rotation of 37.5°; instead, a peak lateral tail-tip displacement of 40.84 mm was found on the right side, with a 37.1° maximum rotation angle, resulting in an asymmetry of approximately 1.07%. At 5 Hz, the maximum leftward and rightward tail-tip lateral displacements were 12.54 and 9.59 mm with corresponding rotations of 14.9° and 11.3°, respectively, resulting in a substantially higher percentage of asymmetry of approximately 27.5%.

Among the key parameters governing fish locomotion, oscillation frequency and tail-beat amplitude play a fundamental role. The forward swimming speed of fish generally increases with both increasing oscillation frequency and increasing tail amplitude. However, as discussed above, the experimental results in water revealed a progressive reduction in bending amplitude as the actuation frequency increased. Consequently, the net effect of an increase in frequency on propulsion capability cannot be assumed a priori, as the beneficial contribution of higher frequency may be partially counterbalanced by the simultaneous reduction in oscillation amplitude.

Since the present prototype is mechanically constrained and not yet capable of free-swimming tests, a direct measurement of forward velocity was not possible. Therefore, a kinematic indicator of propulsion potential was introduced by evaluating the tail-tip mean oscillation speed for each of the six investigated frequencies. This velocity was computed as the ratio between the oscillation amplitude and the time required to complete it.

TABLE 4 | Tail-tip speed as a function of the actuation frequency.

Tail-tip mean speed, mm s^{-1}	Frequency, Hz
88.13	0.50
127.07	1.00
192.55	2.00
187.95	3.00
218.11	4.00
250.80	5.00

The results showed that, in most cases, an increase in the actuation frequency led to an increase in tail oscillation speed (see Table 4).

However, a nonmonotonic trend was observed in the transition from 2 to 3 Hz. At 2 Hz, a tail velocity of 192.55 mm s^{-1} was measured, which is slightly higher than the 187.95 mm s^{-1} recorded at 3 Hz. This indicates that, in this specific frequency range, the reduction in bending amplitude outweighed the increase in oscillation frequency.

Overall, when increasing the actuation frequency by a factor of ten, from 0.5 to 5 Hz, the tail oscillation velocity increased from 88.13 to 250.80 mm s^{-1}, corresponding to an overall increase of approximately 2.85x. These results suggest that, although the progressive reduction in bending amplitude significantly limits performance at higher frequencies, the increase in frequency remains the dominant factor in determining the kinematic tail velocity within the investigated range.

4 | Conclusions

This study presents a manufacturing-integrated soft robotic fish architecture enabled by one-shot multimaterial extrusion.

In this regard, the advantages of multimaterial 3D printing were leveraged to produce a bioinspired design whose body was capable of performing a carangiform swimming motion. In particular, stiff parts like the vertebrae and the caudal fin have been produced in PLA while the compliant spine was manufactured in TPU.

Interlocked T-shaped structures were placed in the middle of each vertebra to achieve and maintain bonding between PLA and TPU across all the tested conditions.

A preliminary investigation was carried out to choose the optimal TPU filament across three different Shore hardnesses available on the market, ranging from 80A to 95A. For that reason, the soft robotic fish was actuated in air (i.e., in the absence of the hydrodynamic load exerted by the surrounding water), finding that an 85A Shore hardness produce the maximum body deflection.

At the same time, a finite element model was formulated to numerically simulate the body deflection. Computational results were in good agreement with in air experiments across all the tested TPU grades, finding a discrepancy of 2.48%, 0.32%, and 2.78% in tip maximum deflection with respect to experimental results obtained when testing the soft robotic fish with compliant parts made of TPU 80A LF, 85A, and 95A, respectively.

Then, electrical measurements were made to establish an additional criterion for the choice of the optimal TPU grade, that is, the minimum power requirement. Findings revealed that the soft robotic fish with compliant parts made of TPU 85A achieves its maximum curvature already at 6.9 V, while using the other TPU grades allowed the design to reach a significantly lower deflection even at 12 V, which is the operating limit for the chosen EM actuators. Moreover, power consumption was reduced by 67.25%, when passing from 12 to 6.9 V of voltage supply. Thermal measurements on the soft robotic fish TPU 85A prototype embedding the EM actuators were done under both voltage values. This analysis underscored the potential to lower the final temperature reached while operating the soft robotic fish in air during a reference time of 5 min, showing a decrease from 92.5°C to 48.4°C, when passing from the highest to the lowest voltage (−47.68%).

These considerations complemented the choice of TPU 85A for further investigations of underwater performance evaluation. Even in this case, the finite element model—this time implementing also the hydrostatic pressure acting on the soft robotic fish—showed good agreement with experimental body curvature.

Then, the soft robotic fish was dynamically tested underwater at the optimal actuation voltage coming from tests in air (i.e., 6.9 V) under six different frequencies, from 0.5 to 5 Hz. It was proved that the maximum deflection reduced with increasing frequency, which is consistent with fish behavior observed in nature. However, both frequency and amplitude determine the theoretical swimming speed. For that reason, the oscillation speed of the tail was estimated, finding that it increases with increasing frequency except in the transition from 2 to 3 Hz, where there is a localized drop in the estimated mean tail-tip oscillation speed. Overall, by augmenting by an order of magnitude the EM actuators' frequency (i.e., from 0.5 to 5 Hz), the tail oscillation velocity increased by less than 3x. This result confirmed that the increase in frequency remains the dominant factor in determining the tail speed even though the reduction in bending amplitude significantly limits performances at the highest frequencies. The proposed robotic fish prototype could be used for underwater exploration, pipeline inspection, and studies in marine biology. However, the electronic components have not been waterproofed yet, and experiments were conducted with an external power supply. Future developments will include waterproofing the onboard electronics, improving the soft fish design to enhance hydrodynamic performance, and incorporating biomimetic features to enable a more natural interaction with real fish.

Funding

The following research work was supported by the following funding sources: BRIEF—Biorobotics Research and Innovation Engineering Facilities—Missione 4, "Istruzione e Ricerca"—Componente 2, "Dalla ricerca all'impresa"—Linea di investimento 3.1, "Fondo per la realizzazione di un sistema integrato di infrastrutture di ricerca e innovazione,"

funded by European Union—Next Generation EU (Grant No. CUP: J13C22000400007); National Recovery and Resilience Plan (NRRP), Mission 4 Component 2 Investment 1.3—Call for tender No. 341 of 15/03/2022 of the Italian Ministry of University and Research funded by the European Union – Next Generation EU (Grant PE00000004), Concession Decree No. 1551 of 11/10/2022 adopted by the Italian Ministry of University and Research (Grant No. CUP: D93C22000920001), MICS (Made in Italy—Circular and Sustainable); and Italian Ministry of University and Research under the Programme "Department of Excellence" Legge 232/2016 (Grant No. CUP: D93C23000100001).

Acknowledgements

Open access publishing facilitated by Politecnico di Bari, as part of the Wiley – CRUI-CARE agreement.

Conflicts of Interest

The authors declare no conflicts of interest.

Data Availability Statement

The data that support the findings of this study are available from the corresponding author upon reasonable request.

References

1. M. Luo, W. Tao, F. Chen, T. K. Khuu, S. Ozel, and C. D. Onal, "Design improvements and dynamic characterization on fluidic elastomer actuators for a soft robotic snake," in 2014 IEEE International Conference on Technologies for Practical Robot Applications (TePRA) (IEEE, 2014), 1–6, https://doi.org/10.1109/TePRA.2014.6869154.

2. X. Qi, T. Gao, and X. Tan, "Bioinspired 3D-Printed Snakeskins Enable Effective Serpentine Locomotion of a Soft Robotic Snake," *Soft Robot* 10, no. 3 (2023): 568–579, https://doi.org/10.1089/soro.2022.0051.

3. X. Qi, H. Shi, T. Pinto, and X. Tan, "A Novel Pneumatic Soft Snake Robot Using Traveling-Wave Locomotion in Constrained Environments," *IEEE Robotics and Automation Letters* 5, no. 2 (2020): 1610–1617, https://doi.org/10.1109/LRA.2020.2969923.

4. E. Gautreau, J. Sandoval, X. Bonnet, M. Arsicault, S. Zeghloul, and M. A. Laribi, "A New Bio-Inspired Hybrid Cable-Driven Robot (HCDR) to Design More Realistic Snakebots," in 2022 International Conference on Robotics and Automation (ICRA) (IEEE, 2022), 2134–2140, https://doi.org/10.1109/ICRA46639.2022.9811550.

5. H. V. Phan and H. C. Park, "Mimicking Nature's Flyers: A Review of Insect-Inspired Flying Robots," *Current Opinion in Insect Science* 42 (2020): 70–75, https://doi.org/10.1016/j.cois.2020.09.008.

6. Z. Tu, F. Fei, and X. Deng, "Untethered Flight of an At-Scale Dual-Motor Hummingbird Robot with Bio-Inspired Decoupled Wings," *IEEE Robotics and Automation Letters* (2020): 1, https://doi.org/10.1109/LRA.2020.2974717.

7. S. M. Youssef, M. Soliman, M. A. Saleh, M. A. Mousa, M. Elsamanty, and A. G. Radwan, "Underwater Soft Robotics: A Review of Bioinspiration in Design, Actuation, Modeling, and Control," *Micromachines (Basel)* 13, no. 1 (2022): 110, https://doi.org/10.3390/mi13010110.

8. X. Jian and T. Zou, "A Review of Locomotion, Control, and Implementation of Robot Fish," *Journal of Intelligent & Robotic Systems* 106, no. 2 (2022): https://doi.org/10.1007/s10846-022-01726-w.

9. R. Wang, C. Zhang, Y. Zhang, W. Tan, W. Chen, and L. Liu, "Soft Underwater Swimming Robots Based on Artificial Muscle," *Advanced Materials Technologies* 8, no. 4 (2023): https://doi.org/10.1002/admt.202200962.

10. R. K. Katzschmann, J. DelPreto, R. MacCurdy, and D. Rus, "Exploration of Underwater Life with an Acoustically Controlled Soft Robotic Fish," *Science Robotics* 3, no. 16 (2018), https://doi.org/10.1126/scirobotics.aar3449.

11. G. Li, et al., "Bioinspired Soft Robots for Deep-Sea Exploration," *Nature Communications* 14, no. 1 (2023): https://doi.org/10.1038/s41467-023-42882-3.

12. F. Berlinger, M. Gauci, and R. Nagpal, "Implicit Coordination for 3D Underwater Collective Behaviors in a Fish-Inspired Robot Swarm," *Science Robotics* 6, no. 50 (2021): https://doi.org/10.1126/scirobotics.abd8668.

13. Z. Wang, L. Wang, T. Wang, and B. Zhang, "Research and Experiments on Electromagnetic-Driven Multi-Joint Bionic Fish," *Robotica* 40, no. 3 (2022): 720–746, https://doi.org/10.1017/S0263574721000771.

14. C. Yan, X. Zhang, Z. Ji, X. Wang, and F. Zhou, "3D-Printed Electromagnetic Actuator for Bionic Swimming Robot," *Journal of Materials Engineering and Performance* 30, no. 9 (2021): 6579–6587, https://doi.org/10.1007/s11665-021-05918-7.

15. Y. Zhong, Z. Li, and R. Du, "A Novel Robot Fish with Wire-Driven Active Body and Compliant Tail," *IEEE/ASME Transactions on Mechatronics* 22, no. 4 (2017): 1633–1643, https://doi.org/10.1109/TMECH.2017.2712820.

16. X. Liao, C. Zhou, Q. Zou, J. Wang, and B. Lu, "Dynamic Modeling and Performance Analysis for a Wire-Driven Elastic Robotic Fish," *IEEE Robotics and Automation Letters* 7, no. 4 (2022): 11174–11181, https://doi.org/10.1109/LRA.2022.3197911.

17. J. Lee, Y. Yoon, H. Park, J. Choi, Y. Jung, S. H. Ko, and W.-H. Yeo, "Bioinspired Soft Robotic Fish for Wireless Underwater Control of Gliding Locomotion," *Advanced Intelligent Systems* 4, no. 7 (2022): https://doi.org/10.1002/aisy.202100271.

18. Z. Chen, X. Tian, X. Chen, B. Wen, and X. Li, "An Experimental Study of the Wire-Driven Compliant Robotic Fish," https://ssrn.com/abstract=4374646.

19. J. Qu, et al., "Recent Advances on Underwater Soft Robots," *Advanced Intelligent Systems* 6, no. 2 (2024): https://doi.org/10.1002/aisy.202300299.

20. R. Martini, Y. Balit, and F. Barthelat, "A Comparative Study of Bio-Inspired Protective Scales Using 3D Printing and Mechanical Testing," *Acta Biomaterialia* 55 (2017): 360–372, https://doi.org/10.1016/j.actbio.2017.03.025.

21. K. Robson Brown, D. Bacheva, and R. S. Trask, "The Structural Efficiency of the Sea Sponge *Euplectella Aspergillum* Skeleton: Bio-Inspiration for 3D Printed Architectures," *Journal of the Royal Society, Interface* 16, no. 154 (2019): 20180965, https://doi.org/10.1098/rsif.2018.0965.

22. C. Walsh Visor, A. Beaudette Harvard Biodesign Lab Tutor, J. Vörös, and E. Zürich, "Development and Evaluation of a Soft Underwater Robot," Semantic Scholar, accessed: Feb 26, (2026).

23. Q. Yang, Q. Wang, Z. Cao, Z. Zhao, Y. Chen, and Y. Zhong, "Development of a Wire-Driven Robotic Fish Based on Double Sine Mechanism," *Biomimetics* 10, no. 3 (2025): 136, https://doi.org/10.3390/biomimetics10030136.

24. Y. H. Lin, et al., "Modeling and Control of a Soft Robotic Fish with Integrated Soft Sensing," *Advanced Intelligent Systems* 5, no. 4 (2023): https://doi.org/10.1002/aisy.202000244.

25. A. Jusufi, D. M. Vogt, R. J. Wood, and G. V. Lauder, "Undulatory Swimming Performance and Body Stiffness Modulation in a Soft Robotic Fish-Inspired Physical Model," *Soft Robotics* 4, no. 3 (2017): 202–210, https://doi.org/10.1089/soro.2016.0053.

26. S. Liu, Y. Wang, Z. Li, M. Jin, L. Ren, and C. Liu, "A Fluid-Driven Soft Robotic Fish Inspired by Fish Muscle Architecture," *Bioinspiration & Biomimetics* 17, no. 2 (2022): 026009, https://doi.org/10.1088/1748-3190/ac4afb.

27. J. Zhou, J.-H. Seo, and R. Mittal, "Hydrodynamically Beneficial School Configurations in Carangiform Swimmers: Insights from a Flow-Physics Informed Model," *Journal of Fluid Mechanics* 1014 (2025): A32, https://doi.org/10.1017/jfm.2025.10303.

28. Heschen, Heschen Solenoid Electromagnet HS-0530B DC 12V 1.7A 5N 10 mm Stroke Push Pull Type Open Frame, Heschen, https://heschen.com/products/hs-0530b-dc12v, accessed: Feb 26, 2026.

29. D. Romano, A. Wahi, M. Miraglia, and C. Stefanini, "Development of a Novel Underactuated Robotic Fish with Magnetic Transmission System," *Machines* 10, no. 9 (2022): 755, https://doi.org/10.3390/machines10090755.

30. M. Ribeiro, O. Sousa Carneiro, and A. Ferreira da Silva, "Interface Geometries in 3D Multi-Material Prints by Fused Filament Fabrication," *Rapid Prototyping Journal* 25, no. 1 (2019): 38–46, https://doi.org/10.1108/RPJ-05-2017-0107.

31. J. Sánchez-Rodríguez, C. Raufaste, and M. Argentina, "Scaling the Tail Beat Frequency and Swimming Speed in Underwater Undulatory Swimming," *Nature Communications* 14, no. 1 (2023): 5569, https://doi.org/10.1038/s41467-023-41368-6.

32. BASF, Technical Data Sheet for Ultrafuse TPU 80A LF, Version 2.0, 14 June 2019, https://3degin.com/images/pdf/80a.pdf, accessed: Feb 26, 2026.

Supporting Information

Additional supporting information can be found online in the Supporting Information section.